

# Tools to detect non-Gaussianity in non-standard cosmological models

J.E. Gallegos<sup>a</sup>, E. Martínez-González<sup>a</sup>, F. Argüeso<sup>b</sup>, L. Cayón<sup>a</sup> and J.L. Sanz<sup>a</sup>

<sup>a</sup>Instituto de Física de Cantabria, E39005, Santander, Spain

<sup>b</sup>Universidad de Oviedo, E33007, Oviedo, Spain

## ABSTRACT

We present a method to detect non-Gaussianity in CMB temperature fluctuations maps, based on the spherical Mexican Hat wavelet. We have applied this method to artificially generated non-Gaussian maps using the Edgeworth expansion. Analyzing the skewness and kurtosis of the wavelet coefficients in contrast to Gaussian simulations, the Mexican Hat is more efficient in detecting non-Gaussianity than the spherical Haar wavelet for all different levels of non-Gaussianity introduced. These results are relevant to test the Gaussian character of the CMB data. The method has also been applied<sup>1</sup> to non-Gaussian maps generated by introducing an additional quadratic term in the gravitational potential.

**Keywords:** Cosmology, Cosmic Microwave Background, Data Analysis, Non-Gaussianity, Wavelet Analysis, Mexican Hat Wavelet, Haar Wavelet

## 1. INTRODUCTION

There is not a unique way to detect and characterize the deviations from Gaussianity that can occur in different ways in random fields. Depending on the kind of features, specific methods will prove to be more efficient than others to extract relevant information on the Gaussian nature of the data which is otherwise hidden. A large number of methods have been already proposed to search for non-Gaussianity in CMB maps. The methods can be grouped by the space in which they act.

In real space the cumulants are standard quantities used to extract information on 1-pdf. Information on the n-pdf can be obtained through the Edgeworth expansion<sup>2</sup> or alternative expansions with a proper normalization.<sup>3</sup> Other quantities focus on topological and geometric statistics, e.g. Minkowski functionals implemented on the sphere<sup>4</sup>; statistics of excursion sets, e.g. characteristics of peaks<sup>5</sup>; also geometrical characteristics of polarization have already been investigated.<sup>6</sup> Multifractal analysis and roughness have been applied to the COBE-DMR data.<sup>7,8</sup>

In Fourier space, the bispectrum has been applied in several occasions to analyze the COBE-DMR data (see e.g. Ferreira et al.<sup>9</sup>) as well as an extension to include possible correlations among multipoles.<sup>10</sup> An alternative approach is to work in eigenspace, extracting the eigenmodes from a principal component analysis; this approach has been taken by Bromley<sup>11</sup> for the COBE-DMR and by Wu et al.<sup>12</sup> for the MAXIMA-1 data. In spite of all this effort there is not any strong evidence of deviations from Gaussianity in the CMB up to date (see, however, Magueijo<sup>10</sup> for a possible deviation).

In this work we concentrate on wavelet space. As it is often pointed out, wavelets are a very useful tool for data analysis due to its space-frequency localization. It has been demonstrated in many applications in a wide variety of scientific fields. In particular, in relation to the CMB the COBE-DMR data has been studied with several wavelet bases acting on the faces of the quad-cube COBE pixelization.<sup>13-15</sup> More appropriate analyses should involve the use of spherical wavelets as in Tenorio.<sup>16</sup> More recently Barreiro et al.<sup>17</sup> and Cayón et al.<sup>18</sup> have convolved the COBE-DMR data with spherical wavelets in the HEALPix pixelization<sup>19</sup> to test the Gaussianity of the data. These works use the Spherical Haar Wavelet (SHW) and the Spherical Mexican Hat

---

Further author information: (Send correspondence to J.E.G.)

J.E.G. : E-mail: jgallego@ifca.unican.es, Address: Instituto de Física de Cantabria, Avda. de los Castros, s/n, 39005 Santander, Spain

Wavelet (SMHW), respectively. We will confront the performance of these two spherical wavelet bases proposed for discriminating between standard inflationary (Gaussian) models and non-Gaussian models which contain artificially specified moments (skewness and kurtosis) in the temperature distribution.

Physically motivated non-Gaussian features can enter in the CMB maps in many ways. Cosmic defects can produce linear discontinuities,<sup>20</sup> hot spots<sup>21</sup> or cold and hot spots.<sup>22</sup> Non-standard inflationary models, e.g. with several interacting scalar fields, are expected to produce a qualitatively different non-Gaussianity. One of the simplest alternative scenarios is based on slow-roll inflation, investigated by Salopek & Spergel<sup>23</sup> and Gangui et al.<sup>24</sup> This model generates non-Gaussianity through features appearing in the inflation potential. The model has been studied by Komatsu & Spergel,<sup>25</sup> Verde et al.<sup>26</sup> and Komatsu et al.<sup>27</sup> The gravitational potential  $\phi(\vec{n})$  includes now a quadratic term with an amplitude regulated by the so called non-linear coupling parameter

$$\phi(\vec{n}) = \phi_L(\vec{n}) + f_{\text{nl}}(\phi_L^2(\vec{n}) - \langle \phi^2 \vec{n} \rangle) \quad (1)$$

where  $\phi_L$  refers to the linear part of the gravitational potential,  $f_{\text{nl}}$  is the nonlinear coupling parameter controlling the amount of non-Gaussianity introduced and the brackets indicate a volume average. Verde et al.<sup>26</sup> conclude in their paper that CMB data will be more sensitive to the non-Gaussianity generated by these models than observations of high redshift objects. Cayón et al.<sup>1</sup> have applied a wavelet space statistic method to simulations of slow-roll inflation model to quantify the probability of non-Gaussianity detections induced by this model.

First we introduce the Spherical Mexican Hat Wavelets (SMHW) and revise the properties of the Spherical Haar Wavelets (SHW). We then describe the simulations of artificially induced non-Gaussianity models used to assess the discriminating power of each wavelet base in pure CMB maps and in the presence of noise. After the discussion of the results from the first part, we discuss the performance of the SMHW to distinguish non-Gaussian models in presence of white noise and refer to the work by Cayón et al.<sup>1</sup> applying the SMHW method to CMB fluctuations maps generated by slow-roll inflation to assess the probability of non-Gaussianity detection from physically motivated models.

## 2. THE SPHERICAL WAVELETS

In recent years wavelets have been used in a wide range of astrophysical applications, in particular, the Mexican Hat wavelet family has been successfully used to extract point sources from CMB maps.<sup>28,29</sup> However, applications of spherical wavelets have been very scarce and limited to a few families of wavelets.

### 2.1. The Mexican Hat on $S^2$

The Mexican Hat wavelet have been extended to the sphere. The extension of this isotropic wavelet is of great interest to CMB analyses. Following a group theory approach, Antoine & Vanderghyest<sup>30</sup> have extended the wavelet on  $S^2$ . This extension incorporates four basic properties:

- a) the basic function is a compensated filter,
- b) translations,
- c) dilations and
- d) Euclidean limit for small angles.

They conclude that the stereographic projection on the sphere is the appropriate one to translate the mentioned properties from the plane to the sphere. Such a projection is defined by  $(\vec{x}) \mapsto (\theta, \phi)$

$$x_1 = 2 \tan \frac{\theta}{2} \cos \phi, \quad x_2 = 2 \tan \frac{\theta}{2} \sin \phi, \quad (2)$$

where  $(\theta, \phi)$  represent polar coordinates on  $S^2$  and  $(y \equiv 2 \tan \frac{\theta}{2}, \phi)$  are polar coordinates in the tangent plane to the North Pole (see Fig. 1).

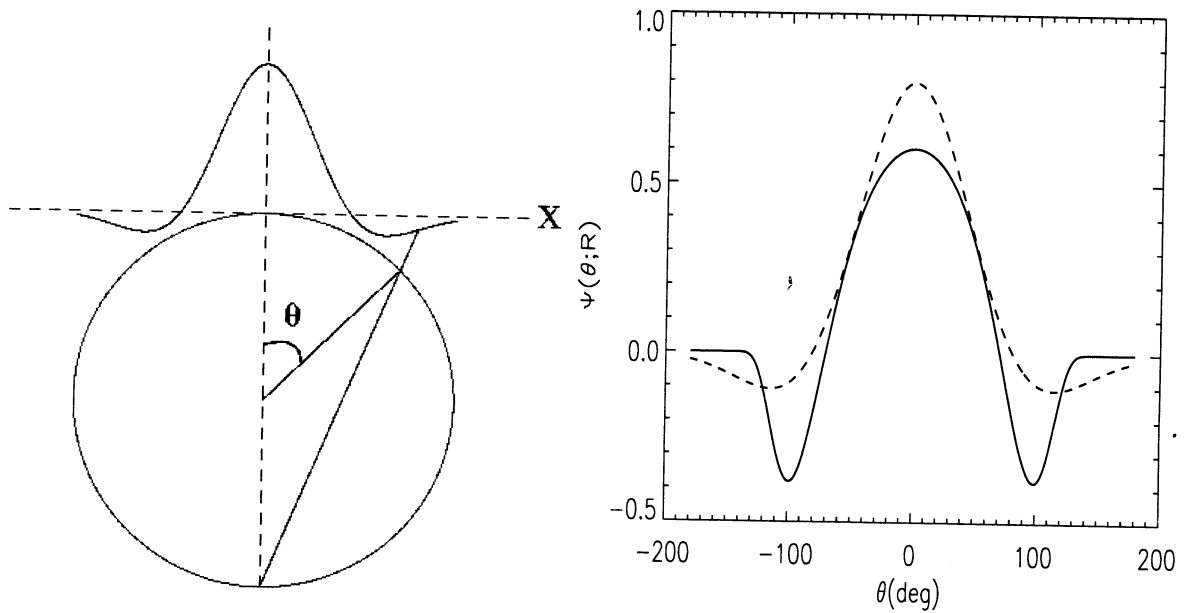


**Figure 1.** LEFT: Stereographic projection to translate the properties of the Mexican Hat Wavelet from the plane to the sphere. RIGHT: Mexican Hat Wavelet as deformed on the sphere (solid line) from the plane (dashed line). The scale of the wavelet is chosen to be  $R = 1$  rad.

Therefore, the isotropic wavelet  $\Psi(x; R)$  transforms to

$$\Psi_S(\theta; R) \propto \left(\cos \frac{\theta}{2}\right)^{-4} \Psi(x \equiv 2 \tan \frac{\theta}{2}; R). \quad (3)$$

It can be proven that the new wavelet on  $S^2$  incorporates the basic properties, i. e. a) it is a compensated filter ( $\int d\theta d\phi \sin \theta \Psi_S(\theta; R) = 0$ ), b) translations are defined by translations along the sphere, i. e. rotations about the center of the sphere, c) the dilations are defined by the stereographic projection of dilations on the plane and d) for small angles one recovers the Euclidean limit.

#### a) Analysis

Let us consider a function on the sphere  $f(\theta, \phi)$ . The continuous wavelet transform with respect to  $\Psi_S(\theta; R)$  is defined as the linear operation

$$\tilde{w}(\vec{x}, R) = \int d\theta' d\phi' \sin \theta' \tilde{f}(\vec{x} + \vec{\mu}) \Psi_S(\theta'; R). \quad (4)$$

$$\vec{x} \equiv 2 \tan \frac{\theta}{2} (\cos \phi, \sin \phi), \vec{\mu} \equiv 2 \tan \frac{\theta'}{2} (\cos \phi', \sin \phi'), \tilde{f}(\vec{x}) \equiv f(\theta, \phi),$$

$w(\theta, \phi; R) \equiv \tilde{w}(\vec{x}, R)$  are the wavelet coefficients dependent on 3 parameters.

#### b) Synthesis

A straightforward calculation based on the equation (5) leads, after stereographic projection, to the continuous reconstruction formula:

$$f(\theta, \phi) \equiv \tilde{f}(\vec{x}) = \frac{1}{C_\psi} \int d\theta' d\phi' \sin \theta' \frac{dR}{R^3} \tilde{w}(\vec{x} + \vec{\mu}, R) \Psi_S(\theta'; R), \quad (5)$$

where  $\tilde{w}(\vec{x}, R) \equiv w(\theta, \phi; R)$ .

### c) The MEXHAT wavelets

A particular example is the MEXHAT wavelet defined by (see Figure 1)

$$\Psi(\theta; R) = \frac{1}{(2\pi)^{1/2} R N} \left[ 1 + \left( \frac{y}{2} \right)^2 \right] \left[ 2 - \left( \frac{y}{R} \right)^2 \right] e^{-y^2/2R^2}, \quad (6)$$

$$N(R) \equiv \left( 1 + \frac{R^2}{2} + \frac{R^4}{4} \right)^{1/2}, y \equiv 2 \tan \frac{\theta}{2}. \quad (7)$$

We remark that the normalization constant has been chosen such that  $\int d\theta d\phi \sin \theta \Psi^2(\theta; R) = 1$ . This is the wavelet we are going to use in this chapter to analyze non-Gaussianity associated to different models. We comment that the stereographic projection of the MEXHAT wavelet has been recently used to analyze maps of the cosmic microwave background radiation (CMB).<sup>18</sup>

## 2.2. Spherical Haar Wavelet

Sweldens<sup>31</sup> introduced the SHW as a generalization of planar Haar wavelets to the pixelized sphere. They are orthogonal and adapted to a given pixelization of the sky which must be hierarchical, contrary to the SMHW which are non-orthogonal and redundant. However they are not obtained from dilations and translations of a mother wavelet, contrary to planar Haar wavelets and SMHW. As for the planar Haar wavelets, they possess a good space-frequency localization. However, their frequency localization is not as good as that of the SMHW. Two applications of SHW to the analysis of CMB maps have already been performed. Tenorio et al.<sup>16</sup> apply them to simulated CMB skies on the QuadCube pixelization. They study the CMB spatial structure by defining a position-dependent measure of power. Also they show their efficiency in denoising and compressing CMB data. Barreiro et al.<sup>17</sup> tested the Gaussianity of the COBE-DMR data on the HEALPix pixelization. One of the advantages of HEALPix over QuadCube is that there is no need to correct for the pixel area.

Since detailed description of the SHW transform has already been given elsewhere, we describe the main features of the wavelet decomposition. The SHW decomposition is based on one scaling  $\phi_{j,k}$  and three wavelet functions  $\psi_{m,j,k}$  at each resolution level  $j$  and position on the grid  $k$ . For HEALPix the resolution is given in terms of the number of divisions in which each side of the basic 12 pixels is divided,  $N_{side} = 2^{j-1}$ . Thus, for level  $j$  the total number of pixels with area  $\mu_j$  is given by  $n_j = 12 \times 4^{j-1}$ . Each pixel  $k$  at resolution  $j$ ,  $S_{j,k}$  is divided into four pixels  $S_{j+1,k_0}, \dots, S_{j+1,k_3}$  at resolution  $j+1$ . For computational reasons the maximum resolution we will consider in our simulations is  $J = 9$  which corresponds to  $N_{side} = 256$ . The scaling and wavelet functions are simply given by

$$\phi_{j,k}(x) = \begin{cases} 1 & \text{if } x \in S_{j,k} \\ 0 & \text{otherwise} \end{cases}, \quad (8)$$

$$\psi_{1,j,k} = \frac{\phi_{j+1,k_0} + \phi_{j+1,k_2} - \phi_{j+1,k_1} - \phi_{j+1,k_3}}{4\mu_{j+1}} \quad (9)$$

$$\psi_{2,j,k} = \frac{\phi_{j+1,k_0} + \phi_{j+1,k_1} - \phi_{j+1,k_2} - \phi_{j+1,k_3}}{4\mu_{j+1}} \quad (10)$$

$$\psi_{3,j,k} = \frac{\phi_{j+1,k_0} + \phi_{j+1,k_3} - \phi_{j+1,k_1} - \phi_{j+1,k_2}}{4\mu_{j+1}} \quad (11)$$

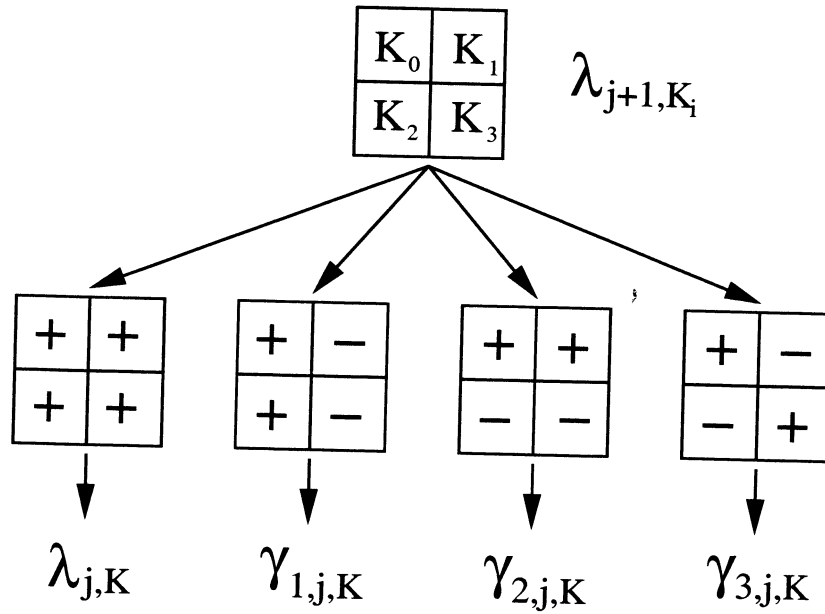


**Figure 2.** Hierarchical structure of Wavelet coefficients for the Spherical Haar Wavelet.

where  $k_0, k_1, k_2, k_3$  are the four pixels at resolution level  $j + 1$  in which the pixel  $k$  at level  $j$  is divided. Please note that the three wavelet functions so defined differ from the ones used by Tenorio et al.<sup>16</sup> and Barreiro et al.<sup>17</sup> We choose those expressions by similarity with the diagonal, vertical and horizontal details defined on the plane. The reconstruction of the temperature field is obtained by

$$\frac{\Delta T}{T}(x_i) = \sum_{l=0}^{n_{j_0}-1} \lambda_{j_0, l} \phi_{j_0, j}(x_i) + \sum_m \sum_{j=j_0}^{J-1} \sum_{l=0}^{n_j-1} \gamma_{m, j, l} \psi_{m, j, l}(x_i), \quad (12)$$

where  $\lambda_{j_0, k}$  and  $\gamma_{m, j, k}$  are the approximation and detail coefficients respectively. The level index  $j$  goes from the finest resolution  $J$  to the coarsest one considered  $j_0$ .

The wavelet coefficients at level  $j$  can be obtained from the four corresponding approximation coefficients at level  $j + 1$ ,  $\lambda_{j+1, k_i}$  as follows (see figure 2.):

$$\lambda_{j, k} = \frac{1}{4} \sum_{i=0}^3 \lambda_{j+1, k_i} \quad (13)$$

$$\gamma_{1, j, k} = \mu_{j+1} (\lambda_{j+1, k_0} + \lambda_{j+1, k_2} - \lambda_{j+1, k_1} - \lambda_{j+1, k_3}) \quad (14)$$

$$\gamma_{2, j, k} = \mu_{j+1} (\lambda_{j+1, k_0} + \lambda_{j+1, k_1} - \lambda_{j+1, k_2} - \lambda_{j+1, k_3}) \quad (15)$$

$$\gamma_{3, j, k} = \mu_{j+1} (\lambda_{j+1, k_0} + \lambda_{j+1, k_3} - \lambda_{j+1, k_1} - \lambda_{j+1, k_2}) \quad (16)$$

The generation of coefficients start with the original map, finest resolution  $j = J$ , for which the coefficients  $\lambda_{J, k}$  are identified with the temperature fluctuation at pixel  $k$ . Finally, from the definition of the SHW it is easily seen that this wavelet is not rotationally invariant, contrary to the SMHW.

### 3. NON-GAUSSIAN SIMULATIONS

There are many ways in which physically motivated non-Gaussian features can enter in the CMB temperature distribution. However, up to now there is no evidence of their existence, being all experimental data consistent with Gaussianity<sup>12, 15, 17, 18, 32</sup> (see however Magueijo<sup>10</sup> for a possible positive signal in the COBE-DMR data, although that detection has not been confirmed by any of the other analyses). If departures from Gaussianity of cosmological origin really exist they will more likely be small and all-sky, sensitive, arcminute resolution experiments will be needed for their detection.

#### 3.1. Edgeworth expansion

Here the spherical wavelets will be tested against non-Gaussian simulations of artificially specified moments that will be assumed to be small. In this case a useful way to construct non-Gaussian distributions is by perturbing the Gaussian one through a sum of moments, the Edgeworth expansion. For simplicity we will consider the two lowest cumulants to characterize the deviations from normality: skewness and kurtosis. As discussed in the introduction alternative models to standard inflation, e.g. cosmic defects as a subdominant source of density perturbations or non-standard inflation, can produce significant levels of at least one of the two moments.

For small deviations from Gaussianity, there is a wide class of distributions that can be given in terms of a Gaussian distribution times an infinite sum of its cumulants. This is the well known Edgeworth expansion. The problem with this expansion is that setting all cumulants to zero except one does not guarantee the positive definiteness and normalization that a distribution has to satisfy. However, for small deviations from normality the resulting function is always positive at least up to many sigmas in the tail of the distribution and the normalization factor required for the function to become a well defined distribution is very small and does not appreciably disturb the non-zero moments (i.e. skewness or kurtosis) introduced in the first place.

The Edgeworth expansion can be obtained from the characteristic function  $\phi(t)$  by considering the linear terms in the cumulants and performing the inverse Fourier transform to recover the density function  $f(x)$ :

$$f(x) = G(x) \left\{ 1 + \sum_{n=3}^{\infty} \frac{k_n}{n! 2^{n/2}} H_n\left(\frac{x}{\sqrt{2}}\right) + O(k_n k_{n'}) \right\} , \quad (17)$$

where  $H_n$  is the Hermite polynomial. Considering the perturbations corresponding to the skewness and kurtosis and keeping only the first terms in the corresponding Hermite polynomials, we have

$$f_S(x) = \frac{e^{-\frac{x^2}{2}}}{\sqrt{2\pi}} \left( 1 + \frac{S}{6} (x(x^2 - 3)) \right) , \quad (18)$$

$$f_K(x) = \frac{e^{-\frac{x^2}{2}}}{\sqrt{2\pi}} \left( 1 + \frac{K}{24} (x^4 - 6x^2 + 3) \right) , \quad (19)$$

where  $S$ ,  $K$  denote skewness and kurtosis, respectively. We will use these equations to generate our artificially specified non-Gaussian distributions. Since the resulting distribution is not well defined even for the case of small skewness and kurtosis we set the function to zero when it becomes negative and we also normalize it appropriately. We remark that the zero cuts of the distribution, if present, appear far away in the tails of the distribution for the case of small values of skewness and kurtosis that we consider here. Also, as a consequence, the normalization value required is very close to 1. In this way we checked that the initial values of the skewness and kurtosis we start with in the Edgeworth expansion does not appreciably change after the necessary changes introduced to obtain a well defined probability density function (pdf).

In order to make the simulations resemble the CMB data observed by a given experiment we smooth them with a Gaussian filter. For practical reasons we use a FWHM of  $33'$  which may correspond to some of the channels in all-sky experiments like MAP and Planck (e.g. the 30GHz channel of the Planck mission). We choose to work on the HEALPix pixelization of the sphere with a resolution  $N_{side} = 256$ . We use the HEALPix package to perform the analysis of our simulated CMB data. However, it is not adequate to use that package to convolve our unfiltered independent temperature data with the Gaussian  $33'$  FWHM beam in Fourier space,

instead we perform the convolution in real space. After that, in order to make the simulations more realistic we normalize the CMB power spectrum  $C_l$  of both Gaussian and non-Gaussian simulations to that of a CDM flat  $\Lambda$ -model (computed with CMBFast) using the HEALPix package. As a consequence of the beam convolution and the introduction of correlations in the temperature maps the original levels of skewness and kurtosis injected through the Edgeworth expansion are reduced (compare columns 1 and 2 in table 1).

#### 4. DISTRIBUTION OF SPHERICAL WAVELET COEFFICIENTS

One nice property of wavelet is that its coefficients represent linear transformations, in the case of a Gaussian distribution the distribution of coefficients remains Gaussian; this allows to test Gaussianity in wavelet space by looking for deviations from normality. However, pixelization of the sphere will introduce biases, which will depend on, for instance, whether the pixels are not of equal area or the distances among neighboring pixels vary with the position on the sphere. The coefficients in the SHW correspond to three different details: diagonal, vertical and horizontal. Since those details are directly obtained from linear operations of the four neighboring pixels, which are not equally separated all over the sphere, correlations present in the temperature fluctuations make the wavelet coefficients biased. This peaks the distribution with respect to a Gaussian and therefore a positive kurtosis appears in the three details of the SHW coefficients, even for temperature realizations derived from normal distributions. There is only one type of coefficients for the SMHW at each scale. Since this is a continuous, rotationally invariant wavelet -and thus not adapted to the pixelization- the distribution is not biased by the pixelization scheme used.

The Edgeworth expansion will be used to introduce different amounts of either kurtosis or skewness and generate Gaussian and non-Gaussian simulations to test the discriminating power of spherical wavelets. This simulations are normalized to a power spectrum  $C_l$  consistent with observations. The skewness and kurtosis are introduced at the highest resolution, so we expect to detect them with the skewness and kurtosis of the high resolution coefficients of the spherical wavelet. Thus we will consider for the analysis the first five resolution scales starting from the finest one. The scales go as powers of 2 for the SHW and for comparison we choose the same values for the SMHW parameter  $R$ : 1, 2, 4, 8 and 16 pixels. We can relate the scales of the two wavelets by looking to the scaling functions. The relation between the side,  $s$ , of the step function (scaling function for the Haar wavelet) and the dispersion  $R$  of the Gaussian is:  $s = \sqrt{2\pi}R$ . Then, for the finest scale  $s = 2$  pixels, which corresponds to an  $R \approx 0.8$  pixels which is approximately 1 pixel. Results obtained in Fourier space are equivalent to those obtained in real space if the functions considered are bandwidth limited (with the bandwidth included in the one covered by the pixelization). We have checked this for the finest resolution of the SMHW. The average difference between the SMHW coefficients computed by direct convolution in real space and going to Fourier space is  $< 1\%$ . Given the 5 values of skewness or kurtosis corresponding to the 5 resolution scales for the SMHW and the 15 values for the SHW (5 scales for each of the 3 details), we would like to construct a test statistic which, combining all this information, can best distinguish between the two hypotheses: a)  $H_0$ : the data are drawn from a Gaussian model, b)  $H_1$ : the data are drawn from a non-Gaussian model with either skewness or kurtosis. The best test statistic in the sense of maximum power for a given significance level is given by the likelihood ratio:

$$t(\vec{x}) = \frac{f(\vec{x}|H_0)}{f(\vec{x}|H_1)} \quad (20)$$

where  $f(\vec{x}|H_0)$  and  $f(\vec{x}|H_1)$  are the pdf of the data given hypotheses  $H_0$  and  $H_1$ , respectively. Since we do not know those multivariate pdfs and would be tremendously costly in CPU time to determine them by Monte Carlo simulations, we use as test statistic the simpler Fisher linear discriminant function<sup>33,34</sup>). This discriminant has been recently used by Barreiro and Hobson<sup>17</sup> to study the discriminating power of planar wavelets to detect non-Gaussianity in the CMB in small patches of the sky. The Fisher discriminant is a linear function of the data that maximizes the distance between the two pdf's,  $g(t|H_0)$  and  $g(t|H_1)$ , such a distance defined as the ratio  $(\tau_0 - \tau_1)^2 / (\Sigma_0^2 + \Sigma_1^2)$ .  $\tau_k$  and  $\Sigma_k^2$ ,  $k = 0, 1$ , are the mean and the variance of  $g(t|H_k)$ , respectively. The Fisher discriminant is given by:

$$t(\vec{x}) = (\vec{\mu}_0 - \vec{\mu}_1)^T W^{-1} \vec{x} \quad (21)$$

with  $W = V_0 + V_1$  and  $V_k$  the covariance matrix and  $\vec{\mu}_k$  the mean values of  $f(\vec{x}|H_k)$ . In the particular case that  $f(\vec{x}|H_0)$  and  $f(\vec{x}|H_1)$  are both multidimensional Gaussians with the same covariance matrix, the Fisher

**Table 1.** Power of the Fisher discriminant at 1% significance level

	Injected	True <sup>1</sup> $\times 10^{-2}$	SMHW P(%)	SHW P(%)	Temperature P(%)
SKEWNESS	0.05	0.9(2.4)	66.8	1.51	2.51
	0.10	1.6(2.3)	100	7.09	4.67
	0.30	4.6(2.4)	100	36.12	36.85
	0.30 <sup>2</sup>	1.1(0.7)	99.6	1.80	2.83
	0.50	6.9(2.4)	100	78.46	73.6
KURTOSIS	0.10	0.3(2.6)	15.35	3.00	1.42
	0.30	0.8(2.7)	86.89	9.00	3.40
	0.40	1.1(2.7)	98.10	16.11	4.90
	0.50	1.4(2.6)	99.90	28.43	3.50
	0.50 <sup>2</sup>	0.2(0.7)	20.84	1.00	0.32

<sup>1</sup> True refers to the mean value obtained in the analyzed maps. The standard deviation is given within parenthesis.

<sup>2</sup> These models include the addition of noise to the maps with  $S/N = 1$ .

discriminant is equivalent to the likelihood ratio. The mean values and covariance matrices of the skewness and kurtosis at each resolution level for the Gaussian and non-Gaussian models are obtained from a large number of simulations. In the next section we use those simulations to compare the power of the test  $p \equiv 1 - \beta$  to discriminate against the alternative hypothesis  $H_1$  at a given significance level  $\alpha$  for the two spherical wavelets.  $\alpha$  and  $\beta$  account for the probability of rejecting the null hypothesis  $H_0$  when it is actually true (error of the first kind) and the probability of accepting  $H_0$  when the true hypothesis is  $H_1$  and not  $H_0$  (error of the second kind), respectively. The decision to accept or reject  $H_0$  is done by defining a critical region for the statistic  $t$ ; if the value of  $t$  is greater than a cut value  $t_{cut}$  the hypothesis  $H_0$  is rejected. Thus,  $\alpha$  and  $\beta$  are given by:

$$\alpha = \int_{t_{cut}}^{\infty} dt g(t|H_0), \quad \beta = \int_{-\infty}^{t_{cut}} dt g(t|H_1). \quad (22)$$

This kind of analysis is very much along the lines of the one performed by Barreiro and Hobson<sup>5</sup> for planar wavelets. From now on a value for the sensitivity of  $\alpha = 1\%$  will be adopted.

## 5. ANALYSIS

Figure 3 summarizes the results and shows the performance of both wavelets detecting non-Gaussianity from artificially non-Gaussian maps generated with the Edgeworth expansion with a kurtosis and skewness of 0.30 in each case; we show the mean values and dispersion of the skewness and kurtosis of the Gaussian and non-Gaussian models for the temperature map, and for the first 5 resolution levels of the SHW diagonal, vertical and horizontal coefficients and SMHW coefficients. As expected the differences are best seen in the finer resolutions. It is clear from Figure 3 that the differences in the skewness for the two models are more remarkable for the SMHW than for the SHW and the temperature map. This is also the case for the kurtosis.

Although there is a bias generated by the pixelization scheme, the Fisher discriminant  $t$  can still be applied to distinguish between the two models. As seen above, what enters in the linear coefficients to compute the statistic  $t$  is the difference between the means from the two models, thus the bias term vanishes. In Figures 4 and 5 we show the probability distribution function for the statistic  $t$  for non-Gaussian models with a skewness and kurtosis of 0.30, respectively; it is clear that for both models the SMHW is able to distinguish between the Gaussian and non-Gaussian models much better than the SHW. In table 1 the power  $p$  of the Fisher discriminant constructed from the skewness or kurtosis of the SMHW, SHW and temperature is given for several values of



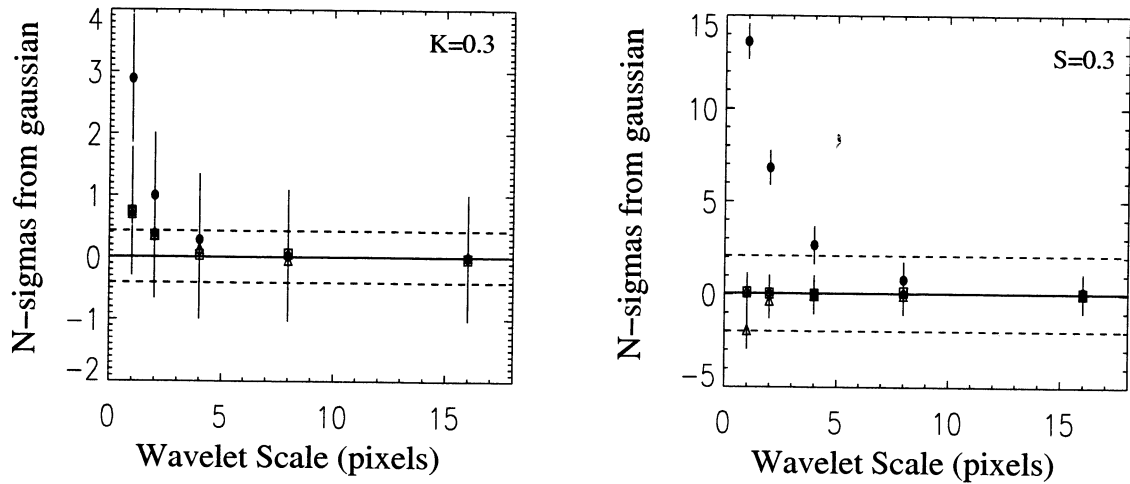


**Figure 3.** Comparison of Mexican Hat wavelet (black circle) and the Haar Wavelet details: Vertical (diamond), Diagonal (triangle) and Horizontal (square); for Kurtosis (left) and Skewness (right) values of 0.30. Each point represents the number of sigmas deviated from the Gaussian model. Also plotted is the stripe for the non-Gaussianity determined from the temperature map (in this case only the pixel scale is meaningful, the stripe is drawn only for illustrative purposes)

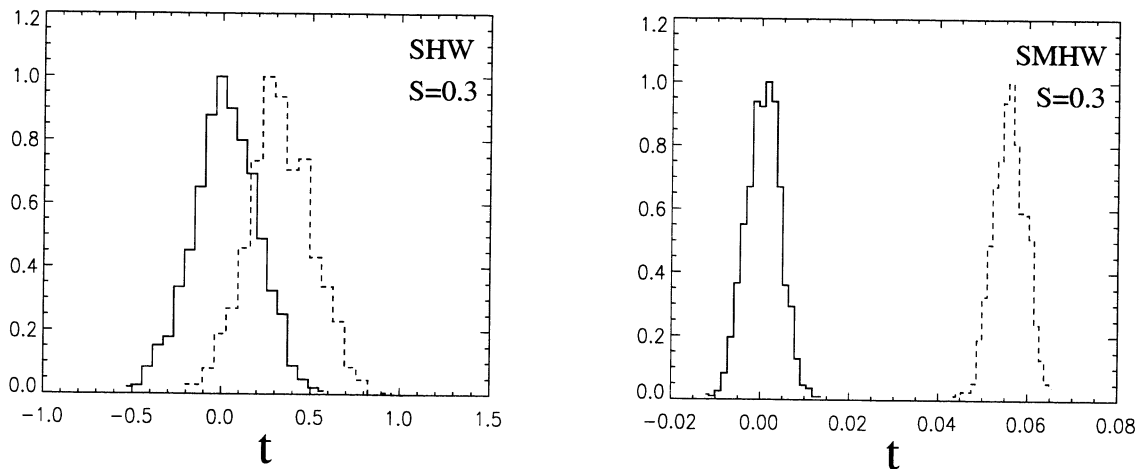


**Figure 4.** Fisher Discriminant for Skewness from Spherical Haar Wavelet (left) and Spherical Mexican Hat Wavelet (right). The value of skewness in the original maps is 0.30. The solid line is the Gaussian model, while the dashed one represents the non-Gaussian case.

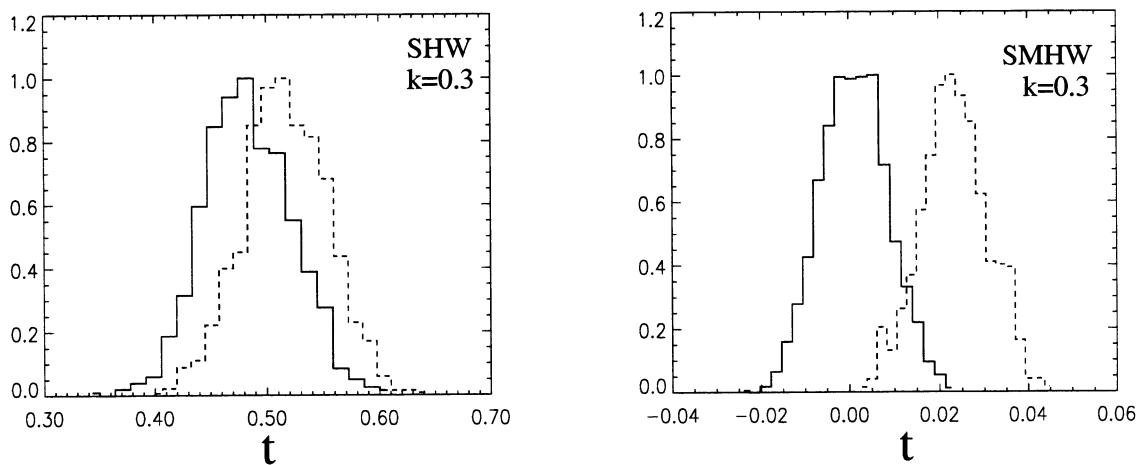


**Figure 5.** Fisher Discriminant for Kurtosis from Spherical Haar Wavelet (left) and Spherical Mexican Hat Wavelet (right). The value of kurtosis in the original maps is 0.30. The solid line is the Gaussian model, while the dashed one represents the non-Gaussian case. Please note the bias in the distribution of the SHW kurtosis as discussed in the text.

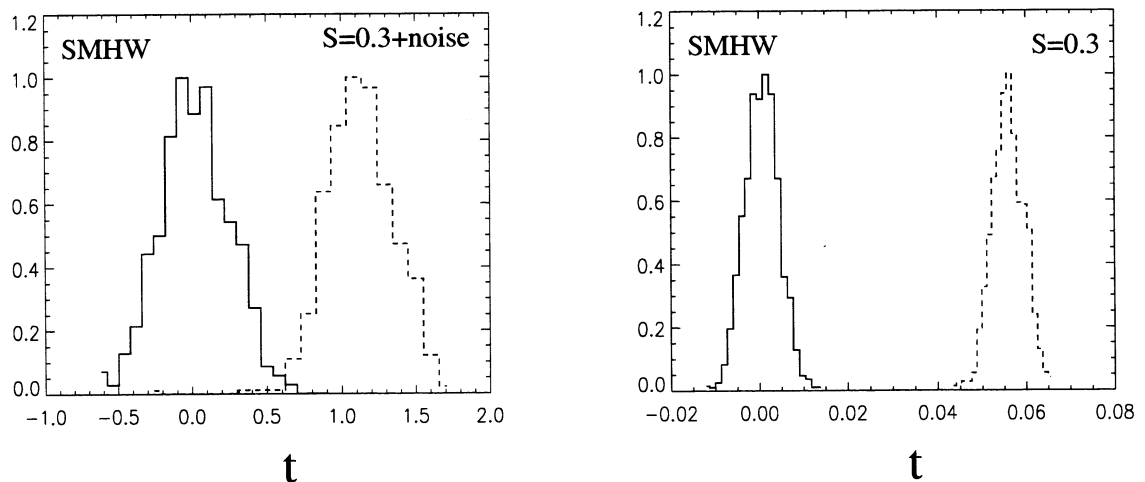


**Figure 6.** The effect of white noise in the discrimination of non-Gaussianity. Depicted is the model with skewness 0.30 with added noise  $S/N=1$  (left) and the clean case (right) for the SMHW.

the cumulants. For the case of the temperature of the map the statistic is given directly by its cumulants. Again, the performance of the SMHW is superior to the SHW and the temperature in all cases. This difference in performance is independent of the fact that the analysis is done on the sphere, equivalent results are obtained on the plane.<sup>35</sup> In the presence of instrumental noise (white) the discriminating power of the spherical wavelets decreases in the first resolution scale, and the second scales becomes the most relevant for discrimination between models. To illustrate the effect of noise, we show in Figure 6 the results for a model with skewness 0.3 with added noise ( $S/N=1$ ) compared with the clean case.

Cayón et al.<sup>1</sup> have tested the SMHW analysis on simulated non-Gaussian low-resolution maps generated from a slow-roll inflation models, with the amount of nonlinearity in the gravitational potential controlled by the nonlinear coupling parameter  $f_{nl}$ . They impose a constraint in the value of the coupling parameter using

the COBE-DMR data of  $|f_{nl}| < 1100$  at the 68% confidence level; this is a tighter constraint than previous ones found by Komatsu et al.<sup>27</sup> using a fit of a non-Gaussian model to the COBE-DMR bispectrum.

## 6. CONCLUSIONS

We present a method based on the Spherical Mexican Hat Wavelet to detect non-Gaussianity which is more efficient than the one based on the Haar wavelet. In particular, the SMHW is able to discriminate a 1.6% skewness with a power of 100% at the 1% significance level whereas the SHW can weakly discriminate a 6.9% skewness with a power of only 78% at the same significance. In the case of kurtosis, the SMHW detects a 1.4% level with a power of 99.9%, while the power for the SHW is only 28%, at the same 1% significance level. An interesting property of the SMHW is that an injected skewness/kurtosis in the temperature maps produces an amplified skewness/kurtosis in the wavelet coefficients and a negligible kurtosis/skewness. In the presence of noise, the highest resolution scale is the most affected and the second scale is then the best one for discrimination. But even in the presence of noise ( $S/N=1$ ) the SMHW is still able to discriminate with a high power levels of skewness and kurtosis above 1% when combining all the information from the different scales with the Fisher discriminant. In a more realistic scenario, the SMHW have been applied by Cayón et al.<sup>1</sup> to CMB maps from models of slow-roll inflation; the SMHW method performs well and has shown successful, setting tighter constraints in the nonlinear coupling parameter using the COBE-DMR data than methods based in the bispectrum.

## REFERENCES

1. L. Cayón, E. Martínez-González, F. Argüeso, A. Banday, and K. Górski *MNRAS*, 2002. submitted.
2. C. Contaldi, P. Ferreira, J. Magueijo, and K. Górski *ApJ* **534**, p. 25, 2000.
3. G. Rocha *et al. astro-ph /0008070*.
4. J. Schmalzing and K. Górski *MNRAS* **297**, p. 355, 1997.
5. R. Barreiro and M. Hobson *MNRAS* **327**, p. 813, 2001.
6. P. Naselsky and D. Novikov *ApJ* **507**, p. 31, 1998.
7. J. Diego, E. Martínez-González, J. Sanz, S. Mollerach, and V. Martínez *MNRAS* **306**, p. 427, 1999.
8. S. Mollerach, V. Martínez, J. Diego, E. Martínez-González, J. Sanz, and S. Paredes *ApJ* **525**, p. 17, 1999.
9. P. Ferreira, J. Magueijo, and K. Górski *ApJ* **503**, p. L1, 1998.
10. J. Magueijo *ApJ* **528**, p. L57, 2000.
11. B. Bromley and M. Tegmark *ApJ* **524**, p. L79, 1999.
12. J. Wu *et al. Phys.Rev.Lett* **87**, p. 251303, 2001.
13. J. Pando, D. Valls-Gabaud, and L. Fang *Phys.Rev.Lett* **81**, p. 4568, 1998.
14. P. Mukherjee, M. Hobson, and A. Lasenby *MNRAS* **318**, p. 1157, 2000.
15. N. Aghanim, O. Forni, and F. Bouchet *A&A* **365**, p. 341, 2001.
16. L. Tenorio, A. Jaffe, S. Hanany, and C. Lineweaver *MNRAS* **310**, p. 823, 1999.
17. B. Barreiro *et al. MNRAS* **318**, p. 475, 2000.
18. L. Cayón, J. Sanz, Martínez-González, *et al. MNRAS* **326**, p. 1243, 2001.
19. K. Górski, E. Hivon, and B. Wandelt, "Analysis issues for large cmb data sets," in *MPA/ESO Conference on Evolution of Large-Scale Structure: from Recombination to Garching*, 1999.
20. N. Kaiser and A. Stebbins *Nature* **310**, p. 391, 1984.
21. D. Coulson *et al. Nature* **368**, p. 27, 1994.
22. N. Turok and D. Spergel *Phys.Rev.Lett* **66**, p. 3093, 1991.
23. D. Salopek and J. Bond *Phys.Rev.D* **43**, p. 3936, 1990.
24. A. Gangui, F. Lucchin, S. Matarrese, and S. Mollerach *ApJ* **430**, p. 447, 1994.
25. E. Komatsu and D. Spergel *Phys.Rev. D* **63**, p. 63002, 2001.
26. L. Verde, R. Jimenez, M. Kamionkowski, and S. Matarrese *MNRAS* **325**, p. 412, 2001.
27. E. Komatsu, B. Wandelt, D. Spergel, A. Banday, and K. Gorski *ApJ* **566**, p. 19, 2001.
28. L. Cayón *et al. MNRAS* **315**, p. 757, 2000.

29. P. Vielva *et al.* *MNRAS* **326**, p. 181, 2001.
30. J.-P. Antoine and P. Vandergheynst *J. Math. Phys.* **39**, p. 3987, 1998.
31. W. Sweldens *Applied Comput. Harm. Anal.* **3**, p. 1186, 1996.
32. A. Kogut *et al.* *ApJ* **470**, p. 653, 1996.
33. R. Fisher *Ann. Eugen* **7**, p. 179, 1936. Reprinted in *Contributions to Mathematical Statistics*, 1950, John Wiley.
34. G. Cowan, *Statistical Data Analysis*, Oxford University Press, 1998.
35. E. Martínez-González, J. Gallegos, F. Argüeso, L. Cayón, and J. Sanz *MNRAS astro-ph/0111284*, 2002.